Dust Properties around the Dust Cloud nearby White Dwarf LAWD 84 in IRIS and AKARI Data

M. S. Paudel

Journal of Nepal Physical Society

Volume 9, Issue 2, December 2023

ISSN: 2392-473X (Print), 2738-9537 (Online)

JNPS, **9** (2): 78-94 (2023)

DOI: https://doi.org/10.3126/jnphyssoc.v9i2.62409

Published by:

Nepal Physical Society
P.O. Box: 2934
Tri-Chandra Campus
Kathmandu, Nepal
Email: nps.editor@gmail.com

JNPS 9 (2): 78-94 (2023)
ISSN: 2392-473X (Print), 2738-9537 (Online)
Research Article *© Nepal Physical Society*
DOI: https://doi.org/10.3126/jnphyssoc.v9i2.62409

Dust Properties around the Dust Cloud nearby White Dwarf LAWD 84 in IRIS and AKARI Data

M. S. Paudel
Department of Physics, Tri-Chandra Multiple Campus, Tribhuvan University, Nepal
Corresponding Email: mspaudel27@gmail.com, madhu.paudel@trc.tu.edu.np

Received: *8th August, 2023;* ***Revised:*** *15th December, 2023;* ***Accepted:*** *26th December, 2023*

ABSTRACT

An isolated dust cloud is discovered nearby the White Dwarf LAWD 84, located at (RA, DEC) (J2000): $21^h19^m36.53^s$, $-55^o50'4.47''$, in the infrared data of Improved Reprocessing of the IRAS (IRIS) and AKARI infrared survey, within angular size $1.0^o \times 1.0^o$. The isolated region of dust cloud is found to be broken into the two parts both in IRIS and AKARI data, named as IRIS-UP, IRIS-LOW, AKARI-UP and AKARI-LOW. The isolated region of flux at 100 μm in IRIS and 140 μm in AKARI is also studied separately. The dust color temperature (T_d) and dust mass (M_d) are calculated from the infrared flux in both data. The average T_d is found to be ~24 K in IRIS data and ~20 K in AKARI data in both parts. The ratio of dust mass in total region to isolated region is found ~ 2.0 in IRIS-UP and AKARI-UP but the ratio is 5.06 in IRIS-LOW and 3.19 in AKARI-LOW clouds. The regression analysis between the infrared fluxes at two wavelength shows a linear relation between the infrared fluxes in both clouds, whereas there is no any preferred relation observed between the infrared flux (both wavelength) and dust color temperature but a direct linear relationship between infrared flux and dust color temperature, and inverse parabolic relationship obtained between the dust color temperature and dust mass in all clouds. The qualitative analysis of contour map of infrared flux, temperature and mass supports this result. Furthermore, the inclination angle of the each clouds, background point sources, Jeans Criteria and Gaussian distribution of the dust color temperature are studied within both clouds to explain the possible ongoing physical phenomenon within the clouds.

Keywords: LAWD 84, Infrared flux, Dust Color Temperature, Dust Mass, IRIS, AKARI.

INTRODUCTION

The development of the infrared astronomy make possible to reach to the deeper part of the interstellar medium enabling the study of the ongoing physical and chemical processes within it. The Infrared Astronomical Satellite (IRAS) was the first space satellite enable to provide the infrared map of the Milky Way galaxy [1]. Even though the interstellar dust is a minor component of the interstellar medium by volume and mass within the galaxy, it has great significance for determining the complex chemical and physical process. The evolution of the interstellar dust itself is under study since major fraction of the dust component can't be accounted by dust evolution model until now. The dominant process of formation of dust is during the AGB phase of the low to intermediate mass star ($M \leq 8M_\odot$) [2, 3]. The strong stellar wind produced in the AGB phase spreads around the center star forming the circumstellar shell. Significant amount of the dust is also produced in the late evolutionary phase of the massive star ($M \geq 25M_\odot$) in the process of the supernova explosion [4, 5, 6]. Once the dust is sprayed within the ISM, it abundance increases by various processes, such as, coagulation, erosion, shattering, etc. [7]

The rotational and vibrational energy level transition of dust molecules causes the emission of the infrared radiation. The physical properties of the dust can be studied by using infrared data. The

Infrared Astronomical Satellite (IRAS), Improved Reprocessing of IRAS Survey (IRIS) [8], AKARI infrared telescope [9], Wide Infrared Survey Explorer (WISE) [10], etc., provides the infrared map of the interstellar medium and a number of research work have been done to study the physical properties of the interstellar dust including the dust color temperature (hereafter T_d) and dust mass (hereafter M_d). The T_d between 20 K to 24 K and M_d is between 10^{28} kg to 10^{29} kg is found within the seven dust sub-structures around the WD 0307+077 using 60 μm and 100 μm infrared images using IRIS [11]. An infrared study of dust clouds around white dwarf PG 1225-079 shows T_d 25.84 K in IRIS, 26.82 K and 27.68 K in AKARI and 291.56 K and 292.46 K in WISE data and M_d is 3.44×10^{28} kg in IRIS, 1.82×10^{26} kg and 5.89×10^{26} in AKARI and 1.12×10^{26} kg and 1.14×10^{26} kg in WISE data [12]. In another study of the dust cloud around Supernova Remnants G053.41+00.3, G053.9+00.2 and G053.1+00.3 the T_d is found 25.66 K and 17.74 K in and M_d is 28.45 $M_\odot$ and 5.01×10^4 $M_\odot$ for IRIS and AKARI data respectively [13]. Within the dust cloud around the white dwarf WD 0352-049 T_d and M_d are found 23.09 K and 1.36×10^{29} kg in IRAS data [14]. An IRAS study around the dust nebula located at Galactic coordinate (353.01^o, 16.98^o) shows T_d 27.92 K and M_d 1.04×10^{29} kg and for dust nebula located at Galactic coordinate (19.42^o, 1.98^o) they are 31.61 K and 5.59×10^{31} kg [15]. In almost all research the range of the T_d is observed between the 15 K and 30 K. There is variation of M_d upto 10^3 times between them because the calculated dust mass is strongly dependent on the distance of the dust cloud and there is wide variation in the value of distance used in these research work, eg., 1667.89 pc for SNRs [13], 32.73 pc for PG1225-079 [12], 399.28 pc for WD 0307+077 [11], 1219 pc for WD 0352-049 [14], 205 pc for WD 2116+675 [16], etc. The distance estimation is one of the major challenges for the dust cloud.

In most of the research work it is seen that the T_d and M_d within the dust cloud have inverse relation, for instance, dust clouds around WD 0352-049 in IRIS data [14], dust cloud around SNRs in AKARI data [13], dust clouds around PG 1225-079 in WISE and AKARI data [12], dust cloud around WD 0011-399 in WISE data [17]. But in some cases it is seen there is no preferred relationship between T_d and M_d for instance, dust cloud around SNRs in IRIS data [13], dust cloud around WD 0011-399 in IRIS and AKARI data [17], dust cloud around PG 1225-079 in IRIS data [12], etc. This contradictory relationship between T_d and M_d needs further investigation for clear explanation. The distribution of temperature within the dust cloud also has a significant impact on the physical ongoing process within the dust clouds. The background sources including the star, young stellar objects, stellar remnants and various ISM components play an important role for determining the distribution of dust color temperature within the dust cloud [13]. The range of temperature within the clouds around WD0307-377 in IRIS data [11], WD 2116+675 in IRAS data [16], dust cavities around the Pulsar in IRIS and AKARI data [18] are found less than 5 K and within the dust clouds around PG 1225-079 in IRIS, AKARI and WISE data [12], SNRs in IRIS and AKARI data [13], WD 011-394 in IRIS, AKARI and WISE data [17] are found to be greater than 5 K. The narrower dust color temperature suggests the thermal stability within the dust clouds.

In this work, an infrared analysis of the dust clouds around the white dwarf LAWD-84 is performed using the data from IRIS and AKARI. The dust color temperature, dust mass is calculated and relationship between flux-temperature-mass is explained. The background sources within the dust clouds, Gaussian distribution of the dust color temperature, Jeans criteria and the inclination angle are calculated and possible results are explained in details.

SOURCES OF DATA

In this works, the data are taken from three different sources. The Flexible Image Transport System (FITS) images of infrared flux in both IRIS [8] and AKARI [9] data are taken from SkyView Virtual Observatory (https://skyview.gsfc.nasa.gov/). The JPEG version of the images at longer wavelength (100 μm in IRIS and 140 μm in AKARI) is shown in Fig. 1. The data from Gaia Space Observatory Early Third Data (Gaia EDR3) [19] are taken from Gaia Archive (https://gea.esac.esa.int/archive/) for the estimation of the distance to the dust cloud. The histogram of the total and selected Gaia EDR3 are shown in Fig. 2. The background sources within the dust clouds are taken from the Set of Identification, Measurement Bibliography for Astronomical Data (SIMBAD) portal (https://simbad.u-strasbg.fr/simbad/sim-fid) [20].

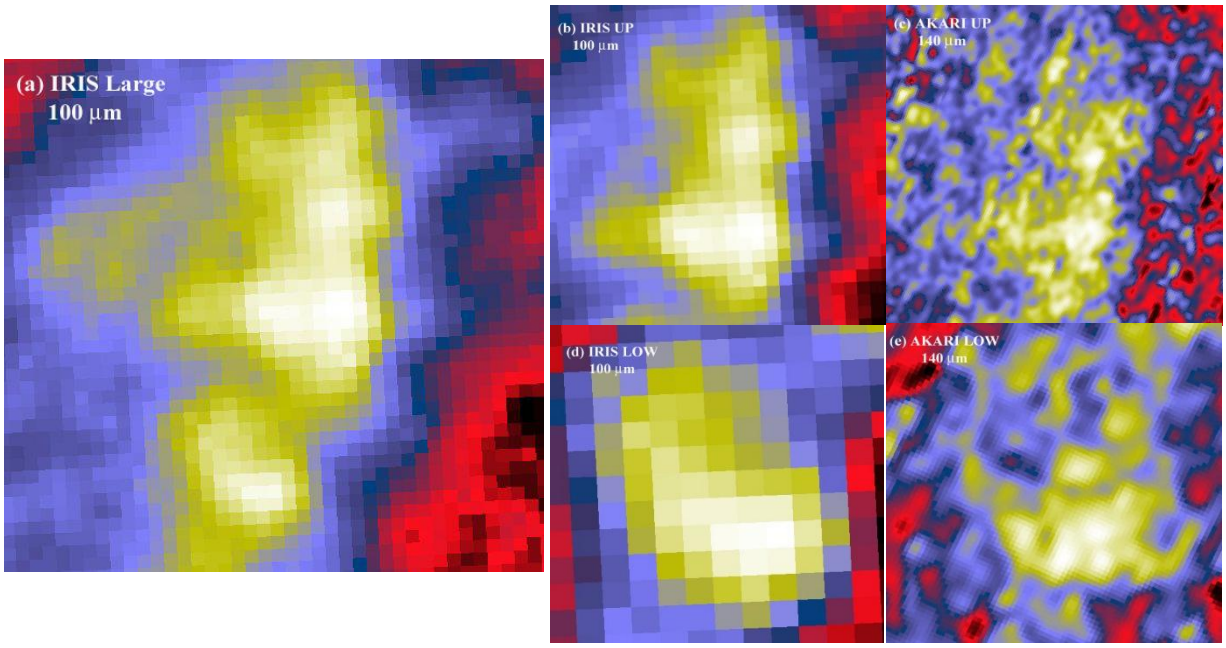

Fig. 1: The JPEG image of the dust cloud nearby the WD LAWD-84 is shown in figure. The figure (a) for large cloud at 100 μm, (b) for IRIS-UP at 100 μm, (c) for AKARI-UP at 140 μm, (d) for IRIS-LOW at 100 μm, and (e) for AKARI-LOW at 140 μm.

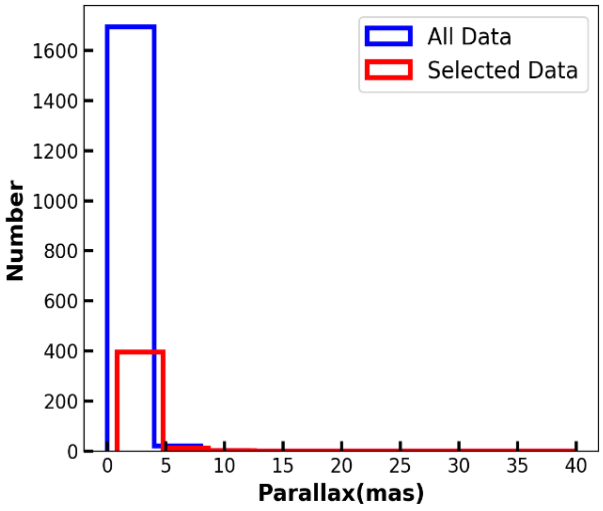

Fig. 2: The histogram parallax of the all and selected Gaia EDR3 sources within $1.0^{o}\times1.0^{o}$ around LAWD-84.

METHOD OF ANALYSIS

Infrared Flux Density

The infrared emission from the interstellar dust is due to the re-emission of the absorbed light. The interstellar dust absorbs the ultra-violet and visible light from the nearby star and stellar objects and re-radiates the energy in infrared band of electromagnetic spectrum. The infrared emission from the interstellar dust depends on the size, temperature, density, etc., of the interstellar dust. With the assumptions that the beam emitted from each pixels in infrared map is isothermal in nature and the beam is in thermal equilibrium along the line of sight, the blackbody emission feature of interstellar dust can be expressed in terms of infrared flux density $F_{\lambda i}$ at wavelength λ_i as; [21, 22]

$$F_i = \left[\frac{2hc}{\lambda_i^3\left(e^{\left(\frac{hc}{\lambda_i k_B T_d}\right)}-1\right)}\right] N_d \alpha \lambda_i^{-\beta} \Omega_i \quad \text{---------- (1)}$$

Where T_d= dust color temperature, N_d = column density of the dust grains, α =constant related to optical depth of the dust, β = spectral emissivity index, Ω_i = solid angle subtended at λ_i by the detector.

The infrared flux at two wavelength can be modified under certain condition to obtain the dust color temperature, which is explained below.

Dust Color Temperature

The ratio (R) of the infrared flux at two wavelength, $F_{\lambda_S}/F_{\lambda_L}$, can be modified under the assumptions that $\Omega_{\lambda_1} \cong \Omega_{\lambda_2}$ and for small dust color temperature, T_d, we obtain,

$$T_d = \frac{-A}{\ln\left[R \times B^{(3+\beta)}\right]} \quad \text{---------- (2)}$$

Where, A is numerical constants with value, A= 96 for IRIS and 57 for AKARI data, and B = λ_S/λ_L = 0.6 for IRIS (λ_S = 60 μm, λ_L = 100 μm) and 0.64 for AKARI data (λ_S = 90 μm, λ_L = 140 μm), β is the spectral emissivity. [22]

The spectral emissivity of the dust grain depends inversely with dust color temperature, given by the Dupac et al., (2003) [23], which is given as;

$$\beta = \frac{1}{(\delta+\omega T_d)} \text{ ----------(3)}$$

Where, δ and ω are the free parameter. The value of β depends on the nature of the interstellar dust, for perfect black body β~0, for amorphous dust β~1 and for dielectric crystal β~2 is taken. In this work, considering the dust grain as dielectric crystalline state, β = 2 is adopted [23].

Dust Mass

For the dust cloud, which is opaque to the visible light, dust mass can be estimated from the infrared emission in addition with the information of the dust grain size, shapes and Planck's function distribution. The long wavelength infrared flux is used for the precise calculation of the dust mass. The expression of dust mass including all these quantities is given as [24, 25];

$$M_{dust} = 0.4\left[\frac{S_\nu D^2}{B(\nu,T_d)}\right] \text{----------(4)}$$

Where, S_ν = absolute value of flux at long wavelength, D = distance to dust cloud, B(ν, T_d) = Planck's function for the blackbody radiation.

The mass of the cloud including cloud is estimated using the relation of the dust to gas ratio, $M_{gas} \approx 200\ M_{dust}$ [25].

Inclination Angle

Inclination angle (*i*) gives the visual impression to the particular celestial body, which is defined as the angle between the line of sight and outward normal to the surface area. The inclination angle is calculated using the Holmberg (1946) [26] formula, given as;

$$cos^2 i = \frac{\left(\frac{b}{a}\right)^2 - (q^*)^2}{1-(q^*)^2} \text{ ----------(5)}$$

Where, *a* and *b* are the size of the major and minor axis of dust cloud and q* is the intrinsic flatness. The intrinsic flatness is the quantity which describes how much amount the internal part of the cloud is opening. Its value is taken 0.23 in this work considering the dust clouds consists of mostly neutral particles [27]. The value of i > 45^o represents *edge-on* and *i* < 45^o represents *face-on* shape of the dust cloud [18].

Jeans Criteria

The Jeans criteria is an important in order to describe whether a particular cloud is likely to collapse via gravitational force leading towards the stellar evolution or not. The Jeans criteria is the criteria on mass and size of the cloud, entirely depending on the density and temperature of the cloud. For a particular cloud of size R, the density of the cloud is given as;

$$\rho = \left(\frac{3}{4\pi}\right)^{2/3} \frac{k_B T}{m_H G R^2} \text{ ---------- (6)}$$

Where, k_B, m_H, *T* and *G* are Boltzmann constant, mass of neutral hydrogen, dust color temperature and universal gravitational constant respectively.

The Jeans mass can be calculates using the relationship;

$$M_J = \left(\frac{k_B T}{m_H G}\right)^{3/2} \frac{1}{\rho^{1/2}} \text{ ---------- (7)}$$

If the Jeans mass of the cloud is less than the total cloud mass then the dust cloud the star formation process can be initiated via the gravitational collapse. [28]

Gaussian distribution

All the natural phenomenon follows the Gaussian distribution. The Gaussian probability distribution function of a random variable x having mean μ and standard deviation σ is given by;

$$F(x) = \frac{1}{\sigma\sqrt{2\pi}} e^{-\frac{1}{2}\left(\frac{x-\mu}{\sigma}\right)^2} \text{ ---------- (8)}$$

RESULT AND DISCUSSION

Structure and Sub-structures

The White Dwarf LAWD-84 is located at RA (J2000): $21^h19^m36.53^s$ and DEC (J2000): -55^{o}50'14.46" [ICRS (RA, DEC): 319.90^o, -55.84^o]. The isolated dust emission structure is prominent and isolated in size 1.0^o×1.0^o, with centered at RA (J2000): $21^h21^m00.15^s$ and DEC (J2000): -56^{o}03'10.2" [ICRS (RA, DEC): 320.25^o, -56.05^o]. The WD LAWD-84 lies at distance 17.20 arcmin along the 43^o with north. Interestingly, the dust structure is prominent in IRIS (60 μm and 100 μm) and AKARI (90 μm and 140 μm) map. The dust

structure breaks into the two part both in IRIS and AKARI. In WISE map more fragmentation of the structure is observed, which is difficult to deal, hence not included within the study.

Furthermore, in close view, the dust structure is found to be split into two segments. They are elongated towards North-South direction and hence divided into upper and lower part. The upper part is named LAWD-84 UP (IRIS-UP in IRIS and AKARI-UP in AKARI data) and lower part is named LAWD-84 LOW (IRIS-LOW in IRIS and AKARI-LOW in AKARI data) throughout this paper. The both dust substructures are studied thoroughly.

The center of the LAWD-84 UP structure is located at RA (J2000): $21^h20^m40.02^s$ and DEC (J2000): $-55^o49'01.0''$ and angular size is $0.65^o \times 0.65^o$ and the center of the LAWD-84 LOW structure is located at RA (J2000): $21^h02^m23.5^s$ and DEC (J2000): $-56^o16'05.6''$ and angular size is $0.30^o \times 0.30^o$. The center of region is represented by geometrical center and the physical center is the point corresponding to the pixels having maximum flux at long wavelength (100 μm in IRIS and 140 μm in AKARI). The geometrical center, physical center, size, total pixels under study and the size of the isolated region of the each sub-structures are presented in the Table 1. The coordinate of the geometrical center and physical center are presented in the ICRS frame of reference. The Aladin v2.5 [29] view of the FITS image at longer wavelength (100 μm in IRIS and 140 μm in AKARI) in all sub-structures are presented in Fig. 3.

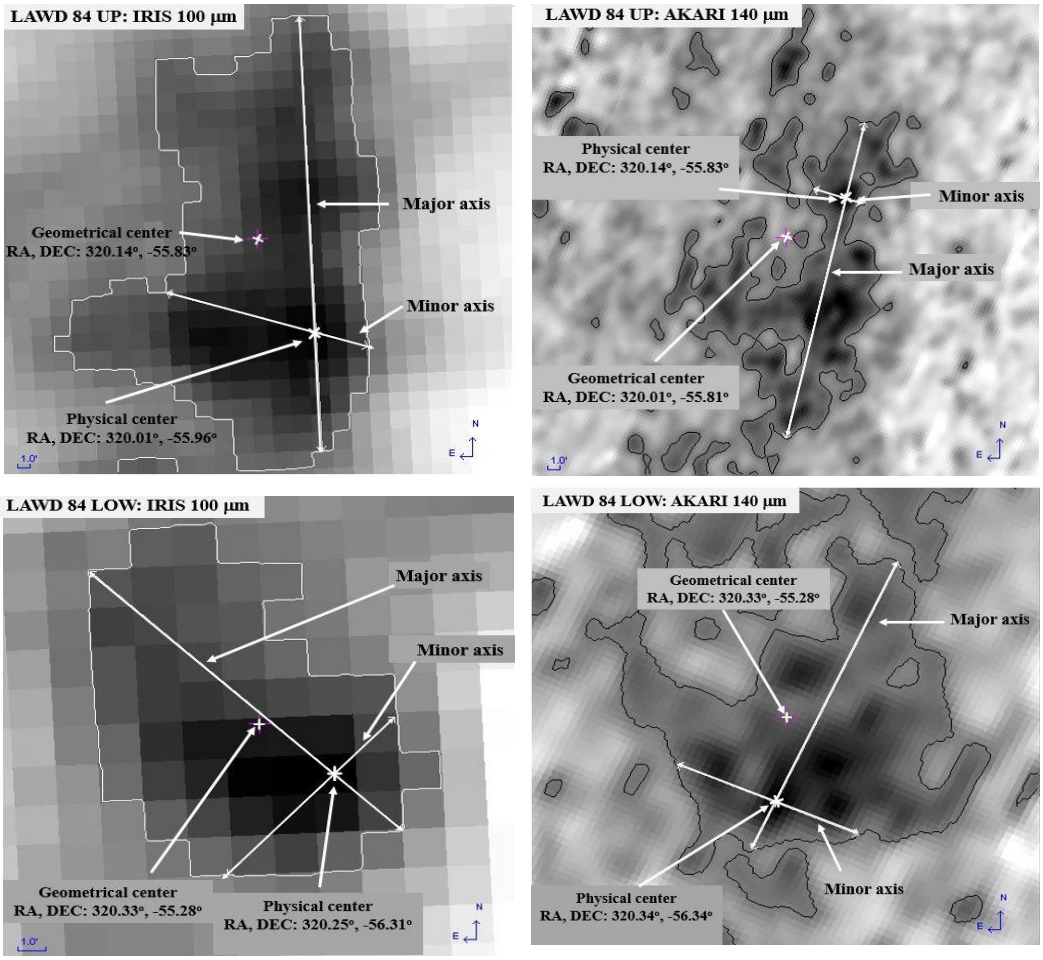

Fig. 3: Figures show the Aladin v2.5 view of the FITS image at long wavelength in both IRIS and AKARI map for both LAWD UP and LAWD LOW cloud. The isocontour isolated region in each cloud. The geometrical and physical center along with major and minor axis are indicated.

Table 1: The table shows center and size of dust sub-structures around WD LAWD-84.

Structure	Geometrical Center (RA, DEC)	Physical Center (RA, DEC)	Total Size	Total Pixels	Size of Isolated Region
IRIS-UP	320.14^o, -55.83^o	320.01^o, -55.96^o	$0.65^o \times 0.65^o$	676	$0.60^o \times 0.28^o$
IRIS-LOW	320.33^o, -55.28^o	320.25^o, -56.31^o	$0.30^o \times 0.30^o$	144	$0.25^o \times 0.15^o$
AKARI-UP	320.14^o, -55.83^o	320.01^o, -55.81^o	$0.65^o \times 0.65^o$	25600	$0.44^o \times 0.07^o$
AKARI-LOW	320.33^o, -56.28^o	320.34^o, -56.34^o	$0.30^o \times 0.30^o$	5184	$0.21^o \times 0.12^o$

Infrared Flux Density

The infrared flux density at two wavelengths, 60 μm and 100 μm in IRIS data and 90 μm and 140 μm in AKARI data are extracted from each pixels of the FITS image. For the extraction of the infrared flux Aladin v11.0 [29] is used. The size and the number of pixels of the all sub-structures are presented in the Table 2. The flux have similar value in both LAWD-84 UP and LAWD-84 LOW structure, in corresponding wavelength. The flux density at AKARI data is higher than in IRIS data. Similar value of infrared flux within the both LAWD-84 UP and LAWD-84 LOW structures indicates that they have identical source and other thermodynamic properties. The statistical information of infrared flux at both wavelengths, 60 μm and 100 μm are presented in Table 2. The error in mean value of flux is the standard error (S.E).

Table 2: Statistical information of infrared flux; maximum (F_{max}), minimum (F_{min}), average (F_{av}), range, standard deviation (σ_F) and standard error (S.E.) at both wavelength in dust structures around WD LAWD 84 in IRIS and AKARI data.

Structure	λ (μm)	F_{max} (MJy/sr)	F_{min} (MJy/sr)	$F_{av} \pm$ S.E. (MJy/sr)	F_{range} (MJy/sr)	σ_F (MJy/sr)
Large (IRIS)	60	2.00	0.70	1.11±3.82e-3	1.29	0.21
	100	8.00	3.22	5.02±0.02	4.78	1.01
IRIS-UP	60	2.00	0.89	1.34±0.01	1.10	0.21
	100	8.00	4.16	6.11±0.03	3.84	0.87
IRIS-LOW	60	1.71	1.21	1.43±0.01	0.50	0.11
	100	7.72	5.52	6.54±0.04	2.20	0.47
AKARI-UP	90	6.87	1.32	3.69±4.49e-3	5.55	0.72
	140	11.46	3.25	6.80±0.01	8.21	1.18
AKARI-LOW	90	6.30	2.53	4.15±0.01	3.77	0.54
	140	11.62	4.63	7.49±0.02	6.99	1.09

Dust Color Temperature

The infrared flux density at two wavelength are used to calculate the dust color temperature following the method of Wood et *al*., (1994) [21] and Schnee *et al*., (2005) [22]. The value of spectral emissivity index β is taken 2 for the crystalline dielectric characteristic of the interstellar dust as suggested by Dupac et *al.*, (2003) [23]. The dust color temperature of the isolated region is calculated separately. The statistical data of dust color temperature large structure and both sub-structure are presented in Table 3. The error given for maximum are minimum temperature are the half of the deviation from average value and error in range are the average of error in maximum and minimum temperature. The error in average temperature is the standard error (S.E.). It is seen that the range of temperature in all structures is less than 4 K in IRIS data. This result suggest that the dust within all the structures is moving towards the thermal stability. But the AKARI data for LAWD

84 UP dust structure is violating this fact, having high range of temperature 5.81 K in isolated region and 10.74 K within total structure. The higher value of T_d for IRIS data compare to AKARI data follows the Wien's displacement law, which is similar to the result for dust around PG 1225-079 [12], dust around SNRs [13], dust around WD0011-399 [17], and dust around Pulsar [18].

Table 3: The table shows the statistical information of dust color temperature; maximum (T_{max}), minimum (T_{min}), average (T_{av}), range, and standard deviation (SD) in total and isolated region of all structure around WD LAWD 84.

Structure	Region	T_{max} (K)	T_{min} (K)	T_{av}± S.E. (K)	T_{range} (K)	σ_T (K)
Large (IRIS)	Total	25.90±0.70	22.28±1.11	23.67±0.01	3.62±0.90	0.45
	Isolated	24.37±0.41	22.62±0.41	23.55±0.01	1.75±0.44	0.31
IRIS-UP	Total	24.92±0.34	22.90±0.68	23.57±0.01	2.02±0.51	0.30
	Isolated	24.35 ±0.35	23.06±0.29	23.64±0.02	1.29±0.32	0.45
IRIS-LOW	Total	24.21±0.32	23.09±0.24	23.57±0.02	1.12±0.28	0.21
	Isolated	23.95±0.18	23.22±0.19	23.57±0.02	0.73±0.18	0.17
AKARI-UP	Total	26.12±3.07	15.38±2.34	20.06±0.01	10.74±2.68	1.05
	Isolated	22.42±1.35	16.61±1.56	19.72±0.01	5.81±1.45	0.83
AKARI-LOW	Total	24.07±1.91	17.59±1.33	20.25±0.01	6.48±1.62	0.90
	Isolated	21.80±1.02	18.16±0.80	19.75±0.02	3.64±0.91	0.65

Relation between Infrared Fluxes

The far-infrared flux at 60 μm and 100 μm in IRIS and at 90 μm and 140 μm in AKARI are used to calculate the dust color temperature. There might be some relation between them. The linear relation is studied using linear regression for total region as well as isolated region, taking the flux at long wavelength (F_L) (100 μm for IRIS and 140 μm for AKARI) along X-axis and flux at short wavelength (F_S) (60 μm for IRIS and 90 μm for AKARI) along Y-axis. Due to small value of coefficient of determination (r^2) compare to total region, the result of best fit for isolated region is not included. The best fit straight line along with the data obtained from FITS image are shown in Fig. 3. The various parameter for best fit straight line are shown in Table 4.

The r^2 value of the best fit line as well as the graph both shows that there is strong linear relation flux at 60 μm and 100 μm in IRIS as expected with r^2 ≥0.80. But for AKARI data, for flux at 90 μm and 140 μm, $r^2 < 0.50$.

The average temperature calculated using the slope of the best fit straight line given in Table 4 are slightly deviated from the average temperature of the total structure presented in Table 3. The difference in temperature (ΔT) between Table 3 and Table 4 is due to the value of y-intercept of the straight line. The large value of y-intercept results more ΔT, for instance; the ΔT for AKARI-LOW is 3.59 K for which the y-intercept is 1.87, where as in IRIS-LOW data ΔT is just 0.21 K and y-intercept is 0.05.

Table 4: The table shows the parameters in linear fit, r^2 is coefficient of determination and T is the dust color temperature calculated using the slope (m).

Structure	Best fit equation	r^2	T (K)
Large (IRIS)	$F_S = 0.20F_L + 0.12$	0.87	22.95
IRIS-UP	$F_S = 0.23\ F_L - 0.06$	0.89	23.82
IRIS-LOW	$F_S = 0.21\ F_L + 0.05$	0.80	23.36
AKARI-UP	$F_S = 0.42F_L + 0.83$	0.48	18.41
AKARI-LOW	$F_S = 0.30\ F_L + 1.87$	0.38	16.66

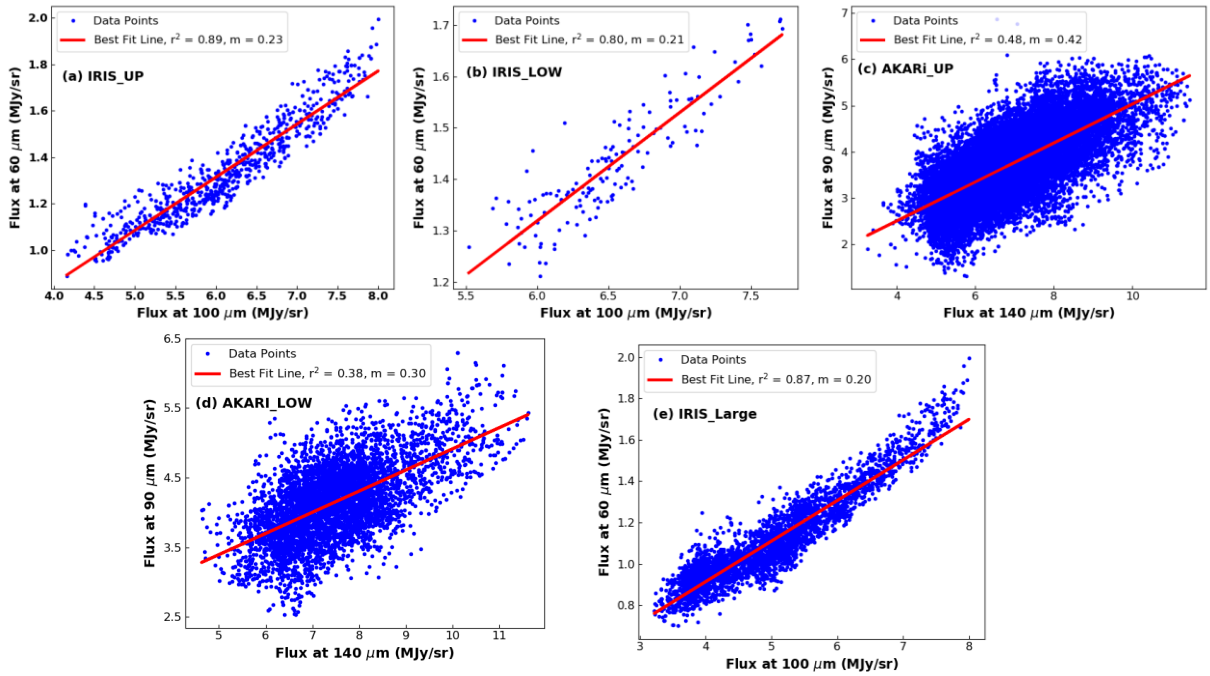

Fig 4: The figure shows the linear relation between two infrared fluxes in IRIS and AKARI data around the WD LAWD84. Here, r^2 is the coefficient of determination and m is slope of straight line.

Dust Mass

The calculation of dust mass is done by following the method of Young *et al.*, (1993) [24] and Hildebrand (1984) [25], for which we need absolute flux, Planck's function and distance. The absolute flux is calculated using the flux density at longer wavelength (100 μm for IRIS and 140 μm for AKARI), Planck's function is calculated using the dust color temperature and value of long wavelength. The distance to the WD LAWD-84 is calculated using the data from GaiaEDR3 [19] from Gaia Archive (https://gea.esac.esa.int/archive), using the value of the parallax of the background sources within the dust structure. The average value of the parallax for selected 410 background objects within $1.0^o \times 1.0^o$ region around WD LAWD-84 is 1.98068 mas, the inverse of parallax gives the distance, which is 504.88 pc. This value is used as a distance to the dust structure and sub-structures around WD LAWD-84 for all calculations. The dust mass as well as the mass of gas within the total square region and isolated region is presented in the Table 5.

Table 5: Dust and Gas mass (kg and solar mass ($M_\odot$)) in dust structure and sub-structures.

Structure	Region	Dust Mass		Gas Mass	
		(in kg)	(in $M_\odot$)	(in kg)	(in $M_\odot$)
Large (IRIS)	Total	1.80×10^{29}	0.09	3.60×10^{31}	18.12
	Isolated	8.00×10^{28}	0.04	1.60×10^{31}	8.05
IRIS-UP	Total	5.55×10^{28}	0.03	1.11×10^{31}	5.58
	Isolated	2.33×10^{28}	0.01	4.67×10^{30}	2.35
IRIS-LOW	Total	1.09×10^{28}	5.49×10^{-3}	2.18×10^{30}	1.10
	Isolated	4.70×10^{27}	2.36×10^{-3}	9.41×10^{29}	0.48
AKARI-UP	Total	2.20×10^{30}	1.10	4.39×10^{32}	220.78
	Isolated	4.35×10^{29}	0.22	8.70×10^{31}	43.76
AKARI-LOW	Total	4.62×10^{29}	0.23	9.23×10^{31}	46.41
	Isolated	1.45×10^{29}	0.07	2.89×10^{31}	14.55

It is seen that the mass of dust is in the same order (~ 10^{28} kg) in both IRIS-UP and IRIS-LOW but for AKARI-UP it is in one order more than in AKARI-LOW, ~10^{30} kg for former and ~10^{29} for later. It is because the size of LAWD-84 UP is larger than LAWD-84 Low. The ratio of the dust mass in total region to the isolated region is found ~2.0 in LAWD-UP in both IRIS and AKARI data, 5.06 in IRIS-LOW and 3.15 in AKARI-LOW. The isolated region in LAWD-84 LOW is found less massive compare to LAWD-84 UP.

Contour Map

The contour map with color plot enables us to distinguish the regions having different magnitude of the various parameter. The contour map with color for the infrared flux density at two wavelength, dust color temperature and dust mass for large dust structure (IRIS data), LAWD 84 UP and LAW 84 LOW sub-structures in both IRIS and AKARI data are presented in Fig.5, Fig. 6, Fig. 7, Fig. 8 and Fig. 9, respectively. In all figure the contour map with color plot are, (a) for flux density at short wavelength (60 μm for IRIS, 90 μm for AKARI), (b) for flux density at longer wavelength (100 μm for IRIS, 140 μm for AKARI), (c) for dust color temperature and (d) for dust mass.

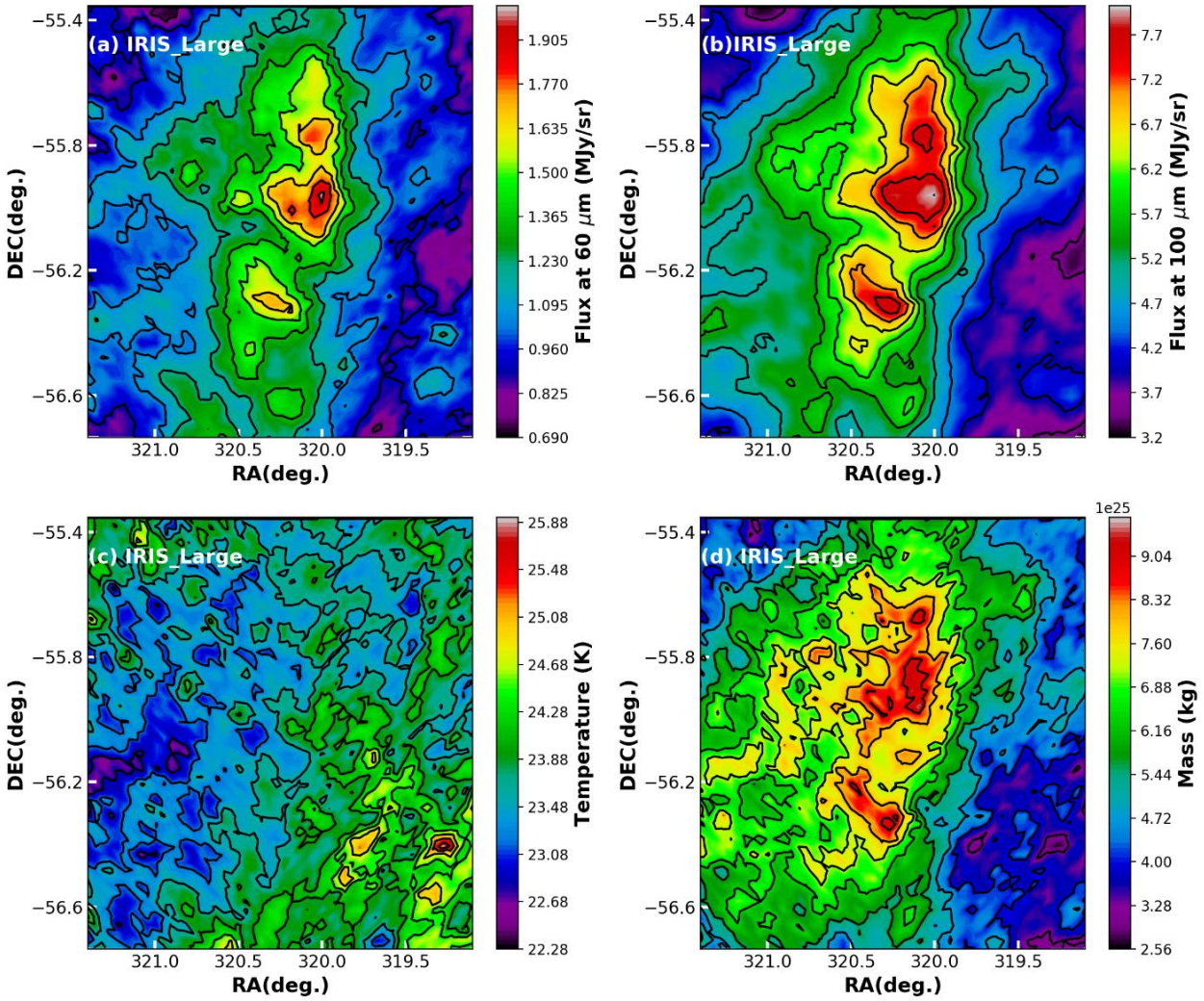

Fig. 5: The contour map for infrared fluxes (a and b), dust color temperature (c) and dust mass (d) for whole dust structure around LAWD 84 in IRIS map.

It is seen that, for all sub-structures the contour plot for flux density at both wavelength looks similar however there is huge difference in the magnitude of flux density. The similar distribution of flux density is also manifested by the linear relation between them (Fig. 4). The aim of the contour map is to find the variation pattern of individual quantity within the dust structure

and to dig out the relationship between two quantities, for example; dust color temperature and infrared flux, dust mass and infrared flux and dust mass and dust color temperature in qualitative way.

The visualization of the contour map of the dust color temperature and infrared flux shows no any correlation between them in all plots. Since, the dust color temperature is estimated from the ratio of the infrared flux, dust color temperature is not seen dependent with individual flux. The contour map of dust mass and infrared flux shows that the variation pattern is almost similar between them. For IRIS data in both UP and LOW structure the association is more clear but in AKARI data in both UP and LOW structure it is somehow a poor association between them. More clearly, it could be seen that the association between the infrared flux and dust mass is effective for long wavelength data, 100 μm for IRIS and 140 μm for AKARI. From the comparison of the contour map of dust color temperature and dust mass it can be seen that there is no any preferred correlation between them in IRIS data but there is inverse relationship in AKARI data both in UP and LOW structure. The exact relationship between them is tried to dig out by studying the r^2 value, presented in the following section.

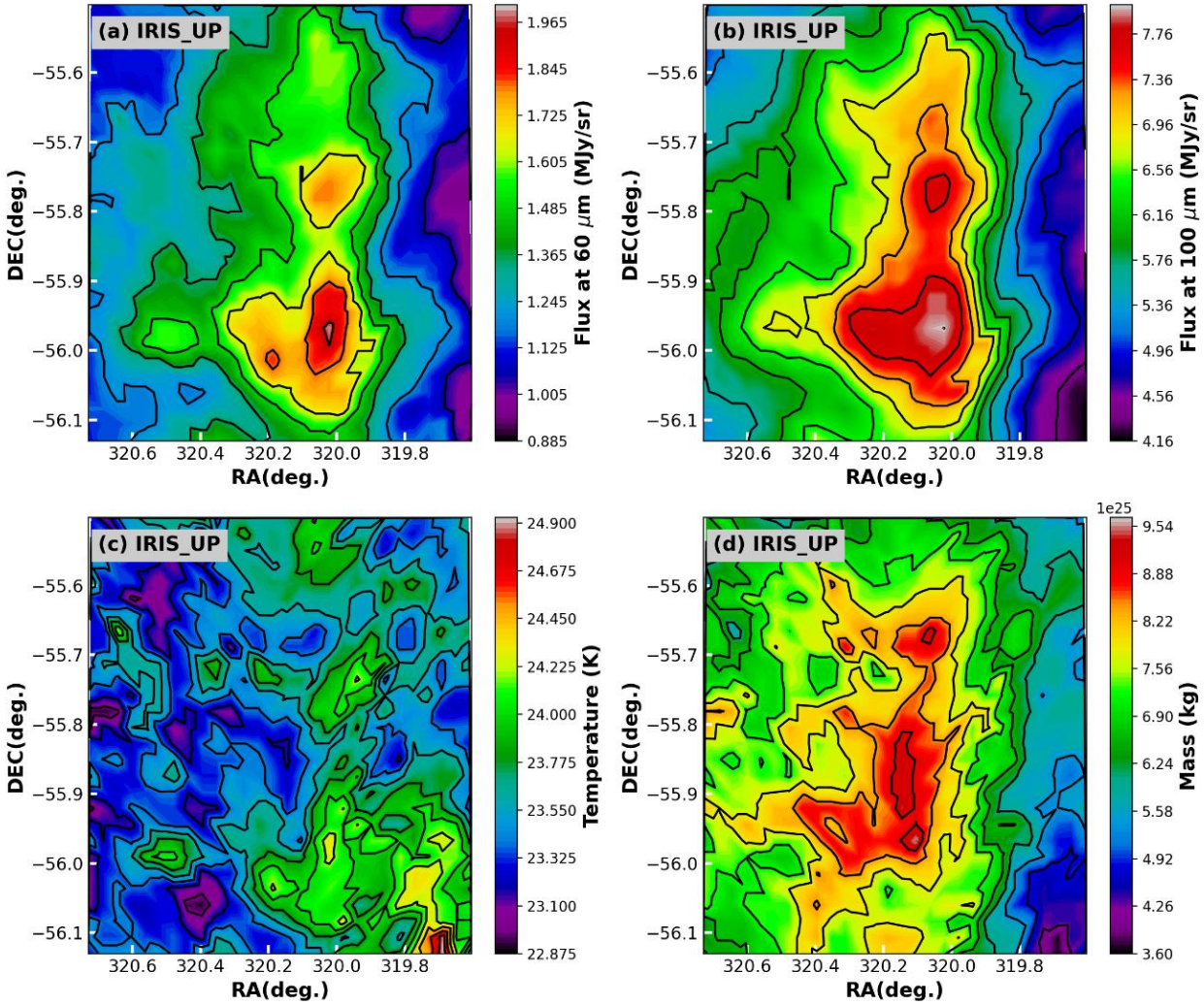

Fig. 6: The contour map for infrared fluxes (a and b), dust color temperature (c) and dust mass (d) for upper dust structure around LAWD 84 UP in IRIS map.

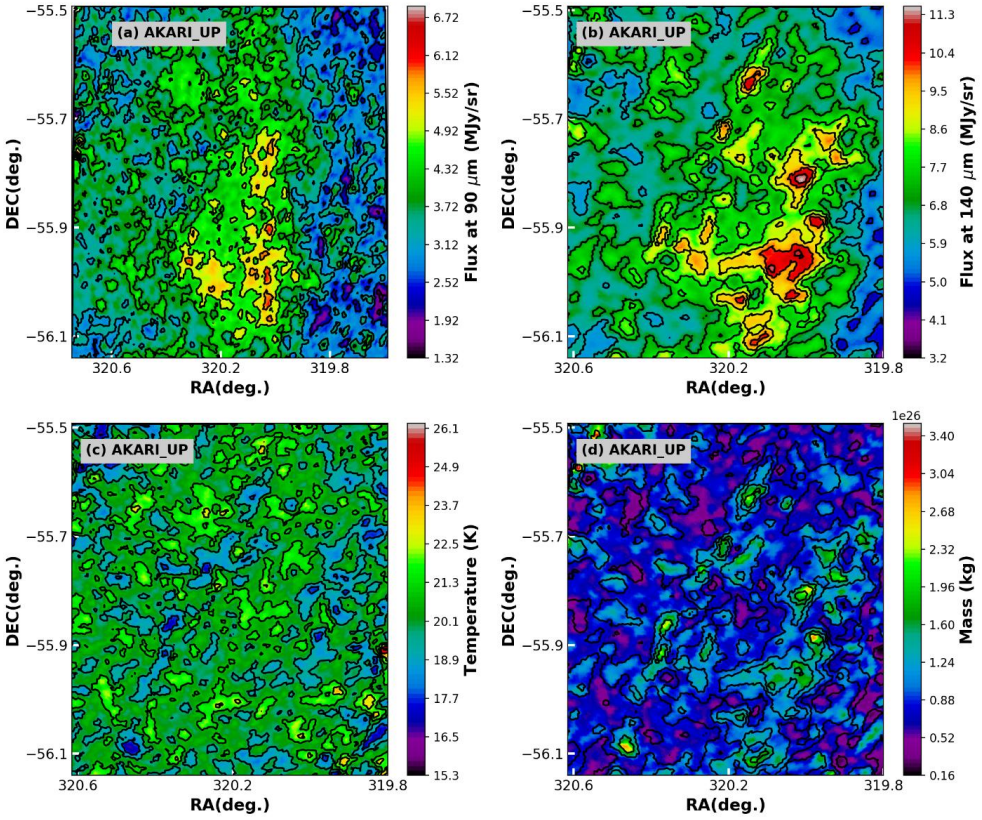

Fig. 7: The contour map for infrared fluxese (a and b), dust color temperature (c) and dust mass (d) for upper dust structure around LAWD 84 UP in AKARI map.

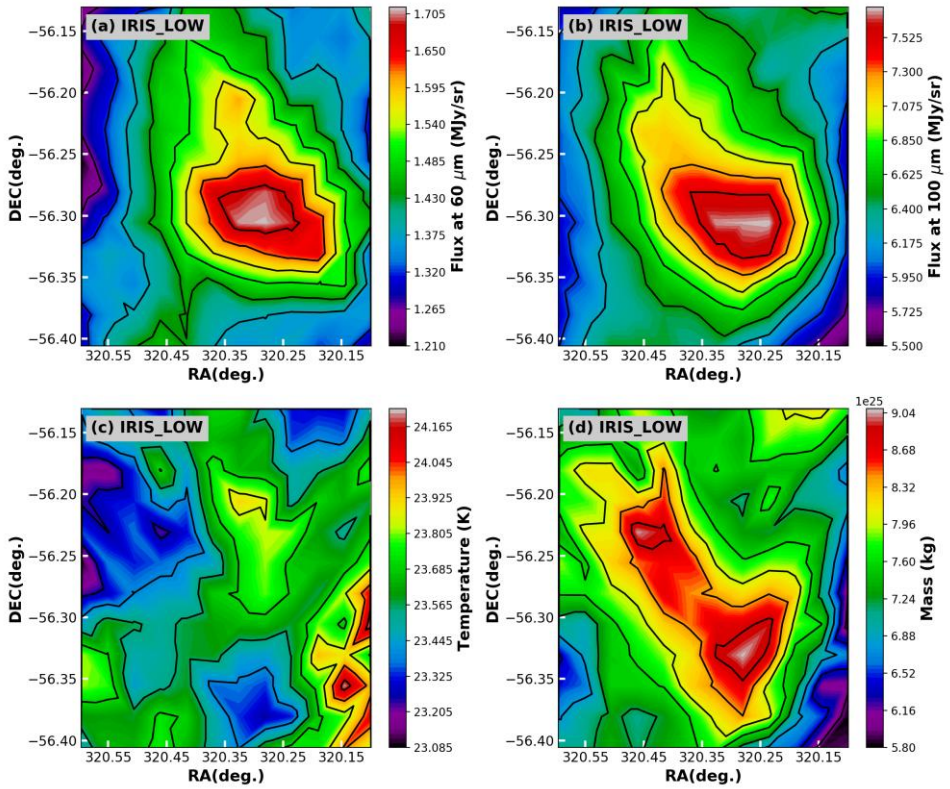

Fig. 8: The contour map for infrared fluxes (a and b), dust color temperature (c) and dust mass (d) for lower dust structure around LAWD 84 LOW in IRIS map.

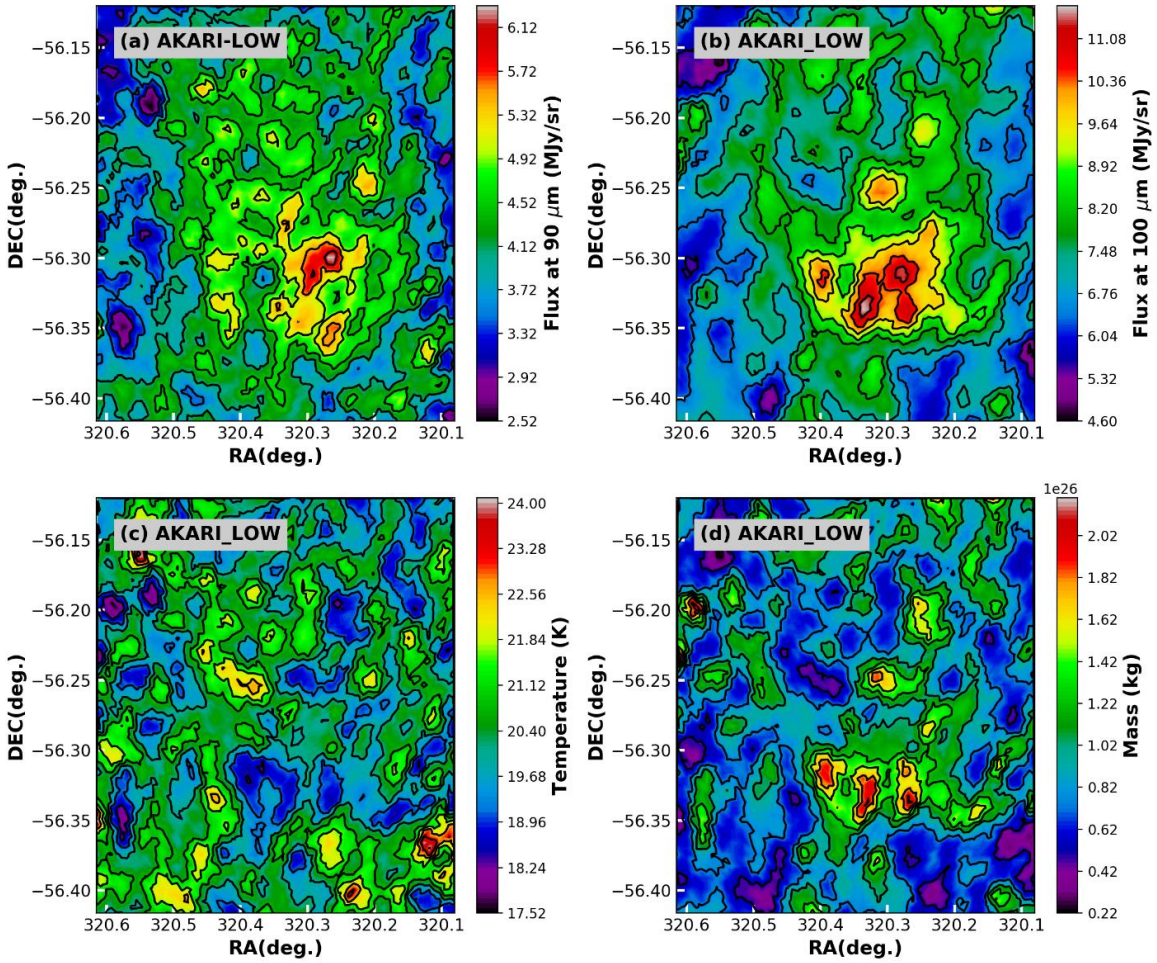

Fig. 9: The contour map for infrared fluxes (a and b), dust color temperature (c) and dust mass (d) for upper dust structure around LAWD-84 LOW in AKARI map.

Flux-Temperature-Mass Relation

The color map of infrared flux, dust color temperature and dust mass couldn't explain the relationship quantitatively. The regression analysis is used to study the exact relation in quantitative way. The relationship between each pair of variables among infrared flux at both wavelength, dust color temperature and dust mass are separately investigated for both (LAWD 84 UP and LOW) structure in both (IRIS and AKARI) data. The selected best fit line estimated using regression analysis, in which the $r^2 \geq 0.50$, is presented below.

For T_d and infrared flux, $r^2 < 0.50$ in both structures in both data. The relationship between the M_d and infrared flux is observed effective only for IRIS-UP, IRIS-LOW and AKARI-LOW, with r^2 value 0.76, 0.68 and 0.64 respectively, as shown in Fig. 10. The linear relation suggest that the increase in dust mass-density along with the increase with the infrared flux. The relationship between M_d and T_d is significant ($r^2 \geq 0.50$) only in AKARI data for both sub-structures, r^2 value 0.76 for UP and 0.82 for LOW. The relationship is found inverse parabolic in nature as shown in Fig. 11. The relation is also inverse in both structure of IRIS. These inverse relation suggest that the cold dust are heavier than hot dust. Moreover, the parabolic decay suggest the rapid decrease in mass-density with increase in temperature. The r^2 coefficient is also given in the each graph. It is direct evident from the study of background objects that there numerous stars within the region under study. They contribute visible radiation for dust for heating there by producing huge thermal radiation near to it. The inverse relation between T_d and M_d is similar to the study of dust around dust clouds around WD 0352-049 in IRIS data [14], dust cloud around SNRs in AKARI data [13], dust clouds around PG 1225-079 in WISE and AKARI data [12], dust cloud around WD 0011-399 in WISE data [17].

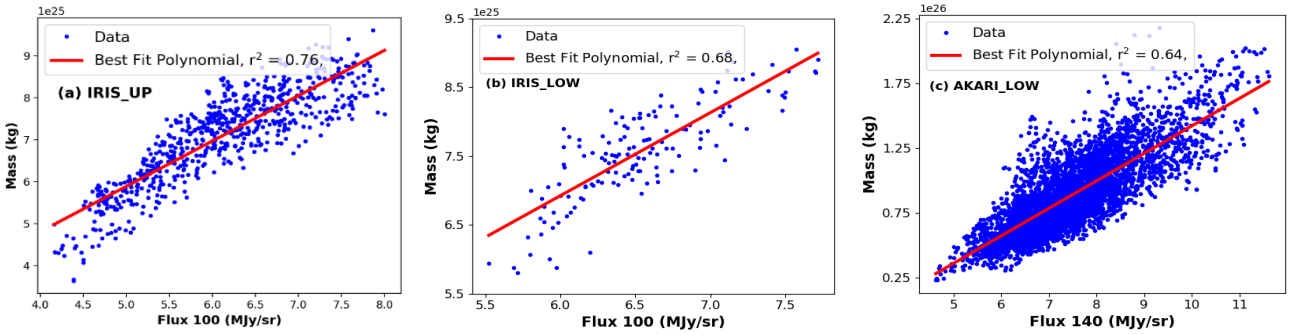

Fig. 10: The best fit straight line between the dust mass and infrared flux for dust cloud around LAWD 84 in IRIS and AKARI data. The good correlation is observed only between these three plots.

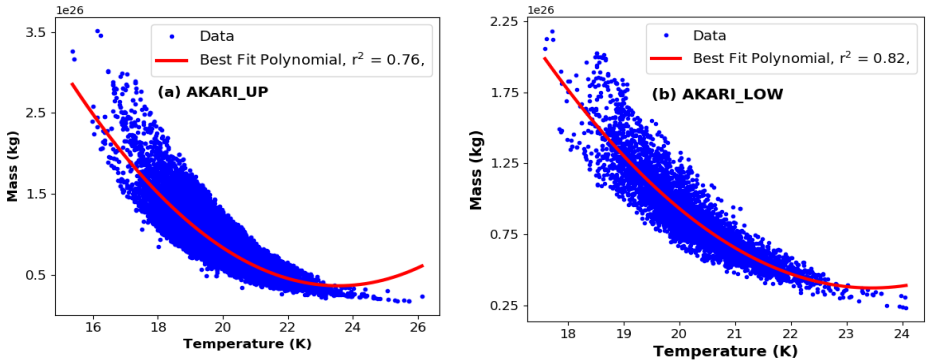

Fig. 11: The best fit second degree parabolic line between the dust color temperature and dust mass for the dust clouds around LAWD 84.

Inclination Angle

The inclination angle of the isolated region of every sub-structures is calculated by using the Holmberg (1946) [26] formula by taking the value of q* equal to 0.23 for molecular cloud [27]. The major and minor axis of the isolated region is calculated by using Aladin v2.5 [29], which is shown in Fig. 3. The major and minor axis are longest and shortest possible lines joining the opposite sides of the isolated region passing from the physical center taking care of that the difference of position angle (PA) is nearly equal to 90^{o}. Table 7 presents the value of major axis, minor axis, position angle of major and minor axis, inclination angle and shape of the cloud. In both sub-structures the inclination angle $i > 45^{o}$ representing the *edge-on* in shape.

Table 6: The table gives the details of major axis, minor axis, position angle (PA) for major and minor axis, inclination angle (i) and the shape of the all clouds.

Structure	Major Axis (arcmin)	Minor Axis (arcmin)	PA Major (deg)	PA Minor (deg)	*i* (deg)	Shape
IRIS-UP	35.83	16.67	2.2	73.6	66.31	edge-on
IRIS-LOW	14.86	8.88	48.0	136.2	55.51	edge-on
AKARI-UP	26.36	3.92	166.7	73.1	90.00	edge-on
AKARI-LOW	12.34	6.94	155.4	66.8	58.20	edge-on

SIMBAD Background Source

SIMBAD enables us to know the objects within the dust structure. The objects around a square region of size $1.0^{o}\times1.0^{o}$ with center at ICRS (RA, DEC): 320.25^{o}, -56.05^{o} are downloaded. The Fig. 12 shows the SIMBAD point objects within the large

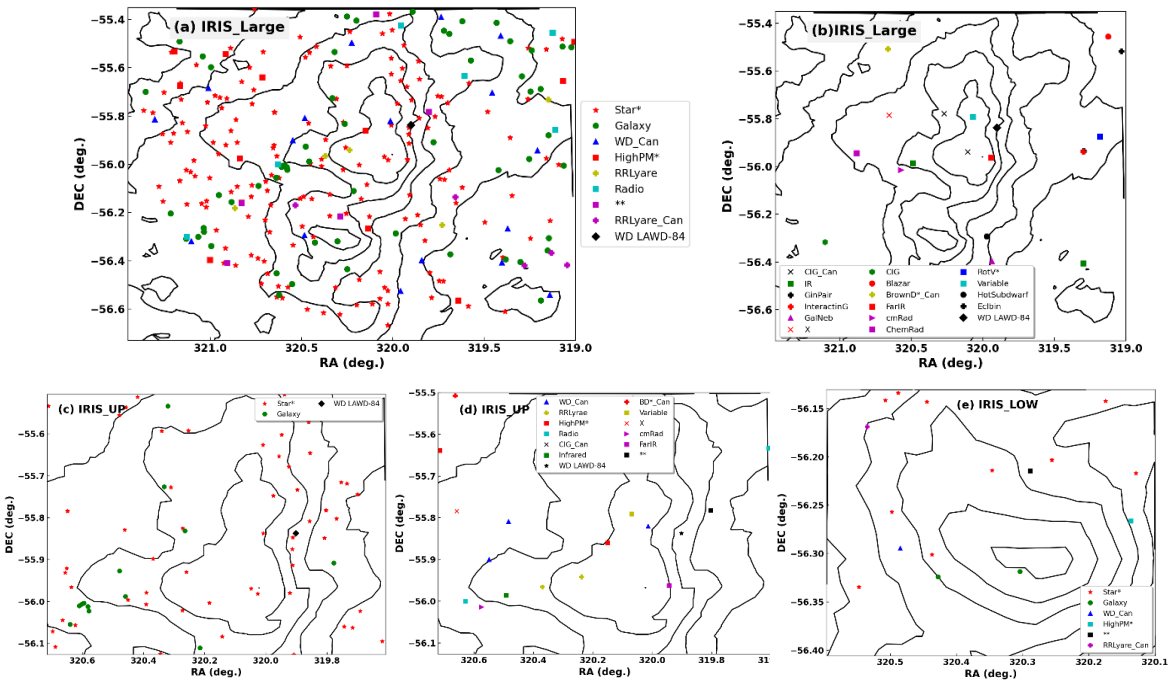

Fig. 12: The figure shows the SIMBAD sources around LAWD 84, for large structure (a and b), LAWD 84 UP (c and d) and LAWD 84 LOW (e). In all plot, RA is taken along X-axis, DEC is taken along Y-axis. The name of sources in the legend is according to the SIMBAD.

dust structures and UP and LOW sub-structures separately. The contour are the isocontour lines for infrared flux at 100 μm. There are total 316 objects within the large structure, 89 objects within the UP and 19 objects within LOW dust structures. The major sources are star and galaxy, which are scattered almost uniformly within all regions. Many sources are only single in number including X-ray and IR sources. The WD LAWD 84 is seen in the left of the UP structure. The effect of presence of the huge stars can be seen in the infrared flux, as we can see huge flux near the center. Not only that, the cold dust is found heavier, which representing the thermal stability near the center of the dust structure. The background point sources plays very important role to regulate the thermal distribution within it.

Density and Jeans Mass

The isolated region of the each cloud under study can be seen in Fig. 3. The mass of the cloud under the isolated structure is sufficient or not to trigger the star formation process is checked out by Jeans criteria. The average size, average temperature, density, Jeans mass and total mass of cloud of isolated region within clouds LAWD 84 UP and LOW are presented in Table 6. The size of LAWD 84 UP is larger than LAWD 84 LOW but density is small. The Jeans mass M_J is greater for LAWD 84 UP cloud. But, the Jeans mass is found larger than the mass of the gas in both structures/clouds. This means, the mass of gas within the cloud is insufficient to initiate the star formation process. It can be concluded that there is no any possibility for the collapse of both clouds for the star formation process in the future.

Table 7: The table shows the average radius, dust color temperature, density, Jeans mass and total mass of cloud in isolated regions of LAWD 84 UP and LAWD 84 LOW.

Structure	Radius (m)	T_d (K)	Density (kg/m^3)	Jeans Mass		Cloud Mass	
				(kg)	($M_\odot$)	(kg)	($M_\odot$)
IRIS-UP	5.90×10^{16}	23.64	3.23×10^{-19}	2.78×10^{32}	139.77	4.67×10^{30}	2.35
IRIS-LOW	2.89×10^{16}	23.57	1.55×10^{-18}	1.27×10^{32}	63.85	9.41×10^{29}	0.48
AKARI-UP	3.43×10^{16}	19.72	7.99×10^{-19}	1.35×10^{32}	67.91	8.70×10^{31}	43.76
AKARI-LOW	2.18×10^{16}	19.75	1.97×10^{-18}	8.61×10^{31}	43.31	2.89×10^{31}	14.55

Gaussian distribution

The Gaussian distribution for dust color temperature and dust mass using IRIS and AKARI data are given below. The Gaussian distribution of the dust color temperature for both LAWD 84 UP and LOW cloud in both survey are more or less

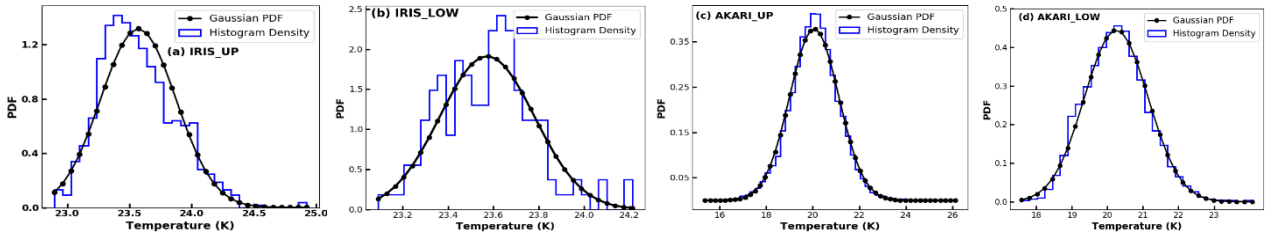

Fig. 12: Figure shows the Gaussian distribution for dust color temperature for all structures. In all figure the quantities dust color temperature is taken along X-axis and their Gaussian PDF are taken along Y-axis.

deviated from the Normal distribution. The deviation might be due to the external point sources within the dust clouds, as shown in SIMBAD database, such as stars. Due to presence of numerous stars there is inhomogeneity in the interstellar medium. That leads to the disruption of the dust cloud leading towards the deviation from normal behavior. The effect is more in IRIS data than the AKARI data due to the presence of more background objects.

CONCLUSIONS

Following are the major conclusions;

1. The dust structure having size $1.0^o \times 1.0^o$ is divided into two sub-structures having size $0.65^o \times 0.65^o$ and $0.30^o \times 0.30^o$ represented as LAWD84 UP and LAWD 84 LOW respectively. Study of Infrared flux shows that the cloud is brighter in AKARI map comparison to IRIS map.
2. The average dust color temperature is found to be ~24 K in IRIS data and ~ 20 K for AKARI data, the temperature difference between the total square region and isolated region is less than 1 K in all dust clouds. Moreover, it is found that the temperature estimated using long wavelength infrared flux (AKARI data) is less compare to short wavelength infrared flux (IRIS data), following the Wien's displacement law.
3. The range of temperature in isolated region is found 1.29 K for IRIS-UP, 0.73 K for IRIS-LOW, 5.81 K for AKARI-UP and 3.64 for AKARI-LOW. In spite of having low average temperature a huge fluctuation is observed in AKARI data. This shows the clouds are more stable in IRIS data compare to AKARI data.
4. The regression analysis shows the linear relationship between the infrared flux at two wavelength, 60 μm and 100 μm in IRIS and 90 μm and 140 μm in AKARI, fitted very well with $r^2 \geq 0.80$ for IRIS data. But for AKARI data they are fitted poorly with $r^2 < 0.50$.
5. The dust color temperature is seen almost independent to the individual infrared flux but the dust mass shows linear relation particularly at longer wavelength. An inverse parabolic relationship is observed between T_d and M_d in AKARI data.
6. The dust mass is in the same order (~ 10^{28} kg) in both IRIS-UP and IRIS-LOW but for AKARI-UP it is in one order more than in AKARI-LOW, ~10^{30} kg for former and ~10^{29} for later. It is because the size of LAWD-84 UP is larger than LAWD-84 LOW. The isolated region in LAWD-84 LOW is found less massive compare to LAWD-84 UP dust cloud.
7. The study of the SIMBAD point sources shows huge number of background objects dominated by stars, which might be responsible for creations of the thermal irregularities within dust cloud. The deviation of the distribution of dust color temperature slightly beyond the normal distribution manifest this fact.
8. The study of the density and Jeans criteria shows the LAWD-LOW cloud is denser than LAWD-UP cloud and in both dust clouds deny the star formation possibility by collapsing the core mass.

ACKNOWLEDGENEMTS

The author wants to acknowledgment to his host institution Department of Physics, Tri-Chandra Multiple Campus for all types of academic support in this research work. This research is fully funded

by University Grants Commission, award no.: SRDIG 77/78 S&T-5, author acknowledges UGC for financial support. Thanks to SkyView Virtual Observatory, SIMBAD and GaiaEDR3 for the availability of data in public platform.

REFERENCES

[1] Neugebauer, G.; Habing, H.; Van Duinen, R.; Aumann, H.; Baud, B. et al. "The infrared astronomical satellite (iras) mission." *The Astrophysical Journal*, **278:** L1–L6 (1984).

[2] Gail H. P.; Sedlmayr E. "Mineral formation in stellar winds. I. Condensation sequence of silicate and iron grains in stationary oxygen rich outflows." *Astronomy & Astrophysics* **347**: 594 (1999).

[3] Ferrarotti, A. S., & Gail, H. P. "Mineral formation in stellar winds-II. Effects of Mg/Si abundance variations on dust composition in AGB stars." *Astronomy & Astrophysics*, **371**(1): 133-151 (2001).

[4] Matsuura, M., et al. "Herschel detects a massive dust reservoir in supernova 1987A." *Science*, **333**: 1258-1261 (2011).

[5] Gomez, H. L.; Krause, O.; Barlow, M.; Swinyard, B.; Owen, P.; Clark, C.; Matsuura, M.; Gomez, E. L.; Rho, J.; Besel, M. A. *et al.*. "A cool dust factory in the crab nebula: a Herschel study of the filaments." *The Astrophysical Journal*, **760**: 96 (2012).

[6] Gehrz, R. D.; Truran, J. W.; Williams, R. E., and Starrfield, S. "Nucleosynthesis in classical novae and its contribution to the interstellar medium." *Publications of the Astronomical Society of the Pacific*, **110** (743): 3 (1998).

[7] Barlow, M. J. "The destruction and growth of dust grains in interstellar space–i. destruction by sputtering," *Monthly Notices of the Royal Astronomical Society*, **183:** 367–395 (1978).

[8] Miville-Deschênes, M. A. and Lagache, G. "Iris: a new generation of iras maps." *The Astrophysical Journal Supplement Series*, **157:** 302 (2005).

[9] Murakami, H.; Baba, H.; Barthel, P.; Clements, D. L.; Cohen, M.; et al. "The infrared astronomical mission akari," *Publications of the Astronomical Society of Japan*, **59**: S369–S376 (2007).

[10] Wright, E. L.; Eisenhardt, P. R.; Mainzer, A. K.; Ressler, M. E.; Cutri, R. M. et al. "The wide-field infrared survey explorer (wise): mission description and initial on-orbit performance." *The Astronomical Journal*, **140:** 1868 (2010).

[11] Paudel, M. S. "Studies of dust properties in substructures around white dwarf wd 0307+077 in iris survey." *Journal of Nepal Physical Society*, **8:** 39–47 (2022).

[12] Sigdel, S.; Rijal, S. and Paudel, M. S. "Comparative Study of dust properties around white dwarf PG 1225-079 in iris and akari survey." *Journal of Nepal Physical Society*, **8** (3): 79–92 (2022).

[13] Paudel, M. S. and Bhattarai, S. "Studies of the properties of dust structure nearby the supernova remnants g053. 41+ 00.3, g053. 9+ 00.2 and g053. 1+ 00.3 using data from iris and akari." *Journal of Nepal Physical Society*, **7**: 59–66 (2021).

[14] Paudel, M. S.; Bhandari, P. and Bhattarai, S. "Study of dust cavity around the white dwarf wd 0352-049 in infrared astronomical satellite map." *Journal of Nepal Physical Society*, **7:** 110–118 (2021).

[15] Thapa, A.; Paudel, M. S. and Pant, B. "An infrared survey of isolated nebular structures at galactic latitudes 16.98° & 1.98° in iras map." *Journal of Nepal Physical Society*, **5**: 74–84 (2019).

[16] Sapkota, B. B.; Aryal, B., and Weinberger, R. "Physical properties of dust particles around white dwarf in far infrared sky at 12.8^{o} galactic latitude." *BIBECHANA*, ***15***, 43-49 (2018).

[17] Rijal, S.; Sigdel, S. and Paudel, M. S. "Study of an isolated dust structure nearby the white dwarf WD0011-399 using iris, akari and wise data." *Journal of Nepal Physical Society*, **8** (2): 14-22, (2022).

[18] Jha, A. and Aryal, B. "A study of a cavity nearby a pulsar at-60º latitude in the far infrared map." *Journal of Nepal Physical Society*, **4:** 33–41 (2017).

[19] Collaboration, G. "Vizier online data catalog: Gaia edr3 (gaia collaboration, 2020)," VizieR Online Data Catalog, I/350 (2020).

[20] Wenger, M.; Ochsenbein, F., Egret, D., Dubois, P., Bonnarel, F., Borde, S., Genova, F.; Jasniewicz, G.; Lalo'e, S.; Lesteven, S., and R. Monier. "The SIMBAD astronomical database-The CDS reference database for astronomical objects." *Astronomy and Astrophysics Supplement Series*, **143**(1): 9-22 (2000).

[21] Wood, D. O.; Myers, P. C. and Daugherty, D. A. "Iras images of nearby dark clouds." *The Astrophysical Journal Supplement Series*, **95:** 457–501 (1994).

[22] Schnee, S. L.; Ridge, N. A.; Goodman, A. A. and Li, J. G. "A complete look at the use of iras emission maps to estimate extinction and dust temperature." *The Astrophysical Journal*, **634**: 442 (2005).

[23] Dupac, X.; Bernard, J. P.; Boudet, N.; Giard, M.; Lamarre, J. M. et al., "Inverse temperature

dependence of the dust submillimeter spectral index." *Astronomy & Astrophysics*, **404**: L11–L15 (2003).

[24] Young, K.; Phillips, T. and Knapp, G. "Circumstellar shells resolved in iras survey data. ii-analysis." *The Astrophysical Journal*, **409:** 725–738 (1993).

[25] Hildebrand, R. H. "The determination of cloud masses and dust characteristics from submillimetre thermal emission." *Quarterly Journal of the Royal Astronomical Society*, **24**: 267 (1983).

[26] Holmberg, E. "On the apparent diameters and the orientation in space of extragalactic nebulae." Meddelanden fran Lunds Astronomiska Observatorium Serie II, **117:** 3–82 (1946).

[27] Haynes, M. P. and Giovanelli, R. "Neutral hydrogen in isolated galaxies. iv-results for the arecibo sample." *The Astronomical Journal*, **89**: 758–800 (1984).

[28] Karttunen, H.; Kröger, P.; Oja, H.; Poutanen, M. and Donner, K. J. Fundamental astronomy. *Springer*, **4: (**2007).

[29] Bonnarel, F.; Fernique, P.; Bienaymé, O.; Egret, D.; Genova, F. et al. "The aladin interactive sky atlas-a reference tool for identification of astronomical sources." *Astronomy and Astrophysics Supplement Series*, **143**: 33–40 (2000).